^{4}He/^{3}He thermochronometry

David L. Shuster *, Kenneth A. Farley

Division of Geological and Planetary Sciences, MC 100-23, California Institute of Technology, Pasadena, CA 91125, USA

Abstract

Using classical diffusion theory, we present a mathematical technique for the determination of ^{4}He concentration profiles in minerals. This approach should prove useful for constraining the low-temperature cooling histories of individual samples and for correcting (U–Th)/He ages for partial diffusive loss. The calculation assumes that the mineral of interest contains an artificially produced and uniform distribution of ^{3}He obtained by proton irradiation [Shuster et al., Earth Planet. Sci. Lett. 217 (2004) 19–32]. In minerals devoid of natural helium, this isotope allows measurement of He diffusion coefficients; in minerals with measurable radiogenic He, it permits determination of ^{4}He profiles arising during ingrowth and diffusion in nature. The ^{4}He profile can be extracted from stepwise degassing experiments in which the ^{4}He/^{3}He ratio is measured. The evolution of the ^{4}He/^{3}He ratio as a function of cumulative ^{3}He released can be compared with forward models to constrain the shape of the profile. Alternatively, we present a linear inversion that can be used to directly solve for the unknown ^{4}He distribution. The inversion incorporates a standard regularization technique to filter the influence of random measurement errors on the solution. Using either approach we show that stepwise degassing data can yield robust and high-resolution information on the ^{4}He profile. Profiles of radiogenic He are a sensitive function of the time–Temperate (t–T) path that a cooling sample experienced. Thus, by step heating a proton-irradiated sample it is possible to restrict the sample's acceptable t–T paths. The sensitivity of this approach was explored by forward-modeling ^{4}He profiles resulting from a range of realistic t–T paths, using apatite as an example. Results indicate that ^{4}He profiles provide rich information on t–T paths, especially when the profiles are coupled with (U–Th)/He cooling ages on the same sample. Samples that experienced only moderate diffusive loss have ^{4}He concentration profiles that are rounded at the edge but uniform in the core of the diffusion domain. Such profiles can be identified by nearly invariant ^{4}He/^{3}He ratios after the first few to few tens of percent of ^{3}He have been extracted by step heating. We show how such data can be used to correct (U–Th)/He ages for partial diffusive loss.

1. Introduction

Helium isotopes are used extensively as chronometers in terrestrial and extraterrestrial materials. ^{4}He produced from radioactive decay of U and Th series nuclides and ^{147}Sm forms the basis of (U–Th)/He chronometry (e.g., [2–5]), while ^{3}He

* Corresponding author. Tel.: +1-626-395-2190;
Fax: +1-626-683-0621.
E-mail addresses: dshuster@caltech.edu (D.L. Shuster),
farley@gps.caltech.edu (K.A. Farley).

produced by cosmic ray spallation is used to estimate surface exposure ages and erosion rates [6,7]. The main attraction of He for these applications is that its production rates are high compared to other isotope systems, coupled with the fact that high-precision, high-sensitivity He analyses are comparatively easy. A critical consideration for these uses is that He diffusion in most minerals occurs at moderate temperatures (250°C–20°C) [5]; failure to consider diffusive loss can lead to erroneously young He-based age constraints. Indeed, this is the primary reason that (U–Th)/He and terrestrial cosmogenic ^{3}He dating have seen only limited application over the last several decades [8] despite considerable analytical advancement [5]. However, if properly characterized, diffusive loss can be used to study low-temperature geologic processes through (U–Th)/He thermochronometry.

Knowledge of He diffusion kinetics is therefore critical for materials in which He measurements are made, particularly for chronometry. Although other methods are sometimes used [9,10], stepwise vacuum outgassing is the most common technique for determining the apparent He diffusivity, D/a^2 (D is the diffusion coefficient, a is the characteristic length scale of the diffusion domain). By measuring the temperature dependence of diffusivity, it is possible to determine the two parameters (activation energy, E_a, and frequency factor, D_o/a^2) which define the Arrhenius function $D(T)/a^2 = D_o/a^2 \ \exp(-E_a/RT)$ required to extrapolate He diffusion coefficients to low temperatures and long time scales over which direct laboratory measurements are impossible.

Vacuum diffusion experiments have several limitations. First, they require sufficient ^{4}He or ^{3}He ($\geq 10^{10}$ and $\geq 10^6$ atoms, respectively) for accurate detection, and so are presently limited to either U-rich phases, old samples, samples that experienced appreciable surface exposure [11] or samples in which He has been introduced by sorption [10]. Current detection limits usually require either large or multiple grains to be analyzed simultaneously, whereas for many applications single-crystal experiments are preferable. A more subtle problem is caused by the initial He distribution within a sample. The rate of diffusive He loss depends on both the diffusivity and the concentration gradient, so converting stepwise release data to diffusivity requires specification of the concentration distribution, $C_o(x,y,z)$, where x, y and z are spatial coordinates [12]. An initially uniform concentration across a spherical diffusion domain, $C_o(r) =$ constant, is typically assumed, where r is radius. This assumption is violated for samples that have experienced He loss either by diffusion or by ejection of α-particles from mineral surfaces following decay. Failure to incorporate such profile rounding in the computation will yield diffusivities that underestimate the true values, potentially by many orders of magnitude. In some cases, an unrecognized rounded profile can yield a remarkably linear Arrhenius array that implies incorrect E_a and D_o/a^2, particularly in the earliest steps.

The goal of previous He diffusion experiments has been to verify He retention in a given material under given conditions (e.g., is cosmogenic ^{3}He quantitatively retained in quartz at 20°C? [11]), or to determine the temperature dependence of diffusivity ($D(T)/a^2$) for thermochronological interpretation [13,14]. As demonstrated by ^{40}Ar/^{39}Ar dating [15], the spatial distribution of a uniformly produced radiogenic noble gas reflects a sample's thermal history. If known, the distribution: (i) permits correction of ages for diffusive loss (i.e., identification of a ^{40}Ar/^{39}Ar age plateau) and (ii) with knowledge of $D(T)$ and the parent nuclide distribution, constrains the thermal history (geologic t–T path) of a sample. Quantitative use of the (U–Th)/He system for these purposes should also be possible. If we determine the *shape* of a ^{4}He concentration profile, the function $D(T)/a^2$ and the U and Th distribution within a sample, we can constrain its t–T path. If we determine the *quantity* of 'missing' He, we can in some cases correct a He age for diffusive ^{4}He loss and/or α-ejection.

Direct measurement of a He distribution is not usually possible. Nuclear reaction analysis and secondary ionization and laser microprobe mass spectrometry lack sufficient sensitivity and/or spatial resolution to measure He concentrations at levels found in most minerals. While ultraviolet laser extraction can be used to measure ^{40}Ar/

[39]Ar profiles [16], high He diffusivities in most minerals make He susceptible to even a small thermal aureole around the ablation pit. Currently the only way to assess the shape of a He concentration profile $C_o(r)$ is to use the indirect approach of stepwise degassing. To determine $C_o(r)$ from stepwise release fractions requires either independent knowledge of $D(T)/a^2$ or a second, uniformly distributed isotope from which $D(T)/a^2$ can be determined [17].

Here we describe how a laboratory-induced, uniform [3]He distribution coupled with an isotope ratio step-heating experiment can be used to determine He diffusivities in *any* mineral and to constrain an unknown natural [4]He distribution using either forward or inverse models. We also examine how thermal histories are recorded in a concentration profile using apatite as an example. In a companion paper we demonstrate applications of this approach following uniform production of [3]He (and negligible [4]He) from all major target elements in minerals via bombardment with a 150 MeV proton beam [1].

2. Theory

2.1. Uniform [3]He distribution

A synthetic and uniform [3]He distribution is useful because: (i) it satisfies the initial condition from which diffusion coefficients are easily calculated [12]; (ii) it allows determination of He diffusivities in minerals that do not contain sufficient natural He for accurate measurement [1]; and (iii) it permits a step-heating experiment in which the [4]He release is normalized to the [3]He released in the same step. Such a *ratio evolution experiment* constrains the initial [4]He distribution.

Unlike [39]Ar in the [40]Ar/[39]Ar method, laboratory-induced [3]He is not uniquely produced from the parent isotopes of [4]He [1], so He isotope release data alone do not define a radiometric age for each step. Instead, such data constrain only the [4]He distribution. With independent knowledge of parent distributions the [4]He profile can be used to correct a He age for diffusive loss, or place t–T constraints on the sample. Because He has only

two isotopes, a 'trapped' He component cannot be identified as it sometimes can in the Ar system [15]. Therefore, this approach is most effectively applied to samples free of excess He in the matrix or inclusions.

2.2. Constraining an initial profile with a stepwise degassing experiment

For reasons discussed below and in [1], it is usually sufficient and simpler to represent a natural [4]He distribution, $C_o(x,y,z)$ by a model radial distribution, $C_o(r)$ within a spherical diffusion domain of equivalent surface area to volume ratio. For a diffusing substance having an initial radial concentration $C_o(r)$ within a spherical diffusion domain $(0 < r < a)$, the concentration at a later time is:

$$C(r, \tau) = \frac{2}{ar}\sum_{k=1}^{\infty}e^{-k^2\pi^2\tau}\sin\left(\frac{k\pi r}{a}\right)\int_0^a r'C_o(r')\sin\left(\frac{k\pi r'}{a}\right)dr' \quad (1)$$

[18] if its mobility follows thermally activated volume diffusion and $C_o(a) = 0$ for all t. We use the non-dimensional diffusion time:

$$\tau(T, t) = \int_0^t \frac{D(T,t)}{a^2}dt \quad (2)$$

Given knowledge of $D(T,t)/a^2$, Eq. 1 describes the distribution $C_i(r)$ after each step $i = \{1,...,n\}$ of a stepwise degassing experiment (either simulated or actual). Considering τ_i to be a piecewise linear, cumulative quantity over the course of an experiment:

$$\tau_i = \sum_i \tau(T_i, t_i) \quad (3)$$

the radial distribution after each step of duration t_i is given by:

$$C_i(r) = C(r, \tau_i) \quad (4)$$

By integrating over the spherical domain, the total amount of diffusant (e.g., [4]He) within the domain after each step i is given by:

$$N_i = \int_0^a 4\pi r^2 C_i(r)dr \quad (5)$$

After each step, the remaining fraction (f) of the original amount of gas is defined as:

$$f_i = \frac{N_o - N_i}{N_o} \qquad (6)$$

where N_o is the original amount. Using the non-dimensional spatial coordinate $x \equiv r/a$, the remaining fraction can also be approximated for values of $\tau < 0.05$ by:

$$f(\tau) = \int_0^1 K(x, \tau)b(x)\mathrm{d}x + \varepsilon \qquad (7)$$

where, after Albarède [19],

$$K(x, \tau) = 3x - 3\left(\mathrm{erf}\frac{1+x}{2\sqrt{\tau}} - \mathrm{erf}\frac{1-x}{2\sqrt{\tau}}\right) \qquad (8)$$

and

$$b(x) = xC_o(x)$$

and ε is the analytical error. Taking Eq. 7 as piecewise continuous in τ such that $f_i = f(\tau_i)$, there exists a direct relation between the sought-after initial profile $C_o(x)$ and the sets of τ_i and f_i in the degassing experiment.

2.2.1. Forward model matching and inversion

If $D(T)/a^2$ is known, these relationships allow us to calculate a set of simulated He remaining fractions, f_i, for any arbitrary initial profile, $C_o(r)$, and heating schedule, τ_i. If the two He isotopes have known relative diffusivity (see below), Eq. 6 can be used to calculate isotope ratios for the concurrent release of a uniformly distributed isotope (^{3}He) and an isotope with an arbitrary natural distribution (^{4}He). This simulates a ratio evolution experiment.

By matching a simulated ratio evolution to experimental observations, forward calculations can be used to constrain $C_o(x)$. In the remaining text, we will refer to this approach as *forward model matching*. In the absence of a uniform ^{3}He distribution, forward model matching to the set of f_i can be used to constrain the shape of a ^{4}He profile, although independent knowledge of $D(T)/a^2$ is required.

As shown by Albarède [17], the above relationships also permit us to directly invert a set of f_i

and an independently determined set of τ_i to solve for $C_o(x)$. With a uniform ^{3}He distribution, and if ^{3}He and ^{4}He have identical diffusivities (or diffusivities that can be quantitatively related to each other), the set of τ_i can be calculated from the ^{3}He release fractions of a step-heating experiment according to [12] and Eq. 3. The set of f_i given by the concurrently determined ^{4}He release fractions can then be used to invert Eq. 7 for $C_o(x)$ as follows.

Eq. 7 is a Fredholm integral equation of the first kind; obtaining the solution $b(x)$ from Eq. 7 is an ill-posed problem [20]. The integral expression can be made arbitrarily discrete in x, thereby defining an $n \times m$ design matrix $\mathbf{K}$ and an $m \times 1$ concentration vector $\mathbf{b}$ ($\mathbf{b} = x_j C_{oj}$), where $i = \{1,...,n\}$, $j = \{1,...,m\}$ and typically, $n < m$. In matrix notation, Eq. 7 can be expressed as:

$$\mathbf{f} = \mathbf{Kb} + \varepsilon \qquad (9)$$

where $\mathbf{f}$ is a column vector of f_i. The model vector $\mathbf{b}$ is a solution of a linear system of equations. The inversion is a discrete ill-posed problem, and may require regularization. Using singular value decomposition to replace $\mathbf{K}$ by $\mathbf{U\Sigma V^T}$ [20], the minimum-norm solution $\mathbf{b}$ (or $\hat{\mathbf{b}}$) of the least squares problem can be calculated by:

$$\hat{\mathbf{b}} = \sum_{i=1}^r \frac{u_i^T \mathbf{f}}{\sigma_i} v_i \qquad (10)$$

where for $n < m$, $\mathbf{U} = (u_1,...,u_n) \in \mathcal{R}^{n \times n}$, $\mathbf{V} = (v_1,...,v_m) \in \mathcal{R}^{m \times m}$, and the first r diagonal elements ($i = j$) of the matrix $\mathbf{\Sigma} \in \mathcal{R}^{n \times m}$ are the non-zero singular values (σ_i) of $\mathbf{K}$ such that $\sigma_1 \geq \sigma_{2...} \geq \sigma_r > 0$, and $r \leq n$. Note that the columns $j > n$ of $\mathbf{V}$ and $\mathbf{\Sigma}$ will be padded with zeros and will not contribute to the estimate $\hat{\mathbf{b}}$.

When working with laboratory data the values f_i will contain analytical errors (ε_i) that limit the information about $\mathbf{b}$ that is invertible from Eq. 9. A threshold index, i_h, can usually be identified as a break in slope if the coefficients $\log(|u_i^T \mathbf{f}|)$ are plotted vs. index i, where for $i > i_h$ the coefficients $|u_i^T \mathbf{f}|$ will be dominated by $|u_i^T \varepsilon|$. These components will dominate $\hat{\mathbf{b}}$, leading to a minimum-norm solution with very large variance [20] and rendering the inversion useless. To avoid this situation, an additional constraint of smoothness

can be used; although this contributes bias to $\hat{\mathbf{b}}$, it will greatly improve the stability of the solution.

In this paper, we use a practical regularization technique called the ridge regression [21,22] (or Tikhonov regularization). The ridge regression uses the filter:

$$w_i = \frac{\sigma_i^2}{\sigma_i^2 + h^2} \tag{11}$$

where the value of h (roughly corresponding to the value of σ_i for $i = i_h$) defines the threshold below which singular values will then insignificantly contribute to the estimate $\hat{\mathbf{b}}$. Under most experimental conditions, the value of h will be determined by analytical uncertainty in f_i. Given the set of w_i, the ridge regression estimate is regularized by:

$$\hat{\mathbf{b}} = \sum_{i=1}^{n} w_i \frac{u_i^T \mathbf{f}}{\sigma_i} v_i \tag{12}$$

Therefore, within analytical uncertainty a stable solution $\hat{\mathbf{b}}$ can be calculated from a combined ^{3}He and ^{4}He diffusion experiment. The ^{3}He results yield $D(T)/a^2$ (i.e., define the set of τ_i) and the measured f_i are determined from ^{4}He release. The profile $C_o(x)$ can then be calculated from $\hat{\mathbf{b}}$. A consequence of regularization is degradation of the resolution kernels, which ultimately limits the amount of information that can be retrieved by the inverse calculation [20].

2.3. Chronometric implications of the initial profile

We now consider two potential uses of a natural ^{4}He profile revealed by the techniques described above: (i) to quantify and correct for the fraction of He removed by diffusion and α-ejection, and (ii) to constrain sample t–T paths. Our goal is to evaluate the sensitivity of the ^{4}He profile for each of these applications.

It is useful to compare the total amount of diffusant in a rounded profile (N_o, Eq. 5) with the amount in a uniform profile (N_{uniform}) with concentration equivalent to that of a quantitatively retentive material. We define the *deficit gas fraction* as $(N_{\text{uniform}} - N_o)/N_{\text{uniform}}$. In certain instances, this quantity can be used to correct an absolute He age for diffusive and α-ejection

loss. An important caveat to this correction is that diffusion and α-ejection have not removed helium from the center of the domain, when $N_{\text{uniform}} = 4/3\pi a^3 C_o(r = 0)$. This case will generally be met for deficit gas fractions $< 50\%$ and might apply, e.g., to volcanic phenocrysts and low-temperature precipitates that partially retain He under Earth surface conditions.

With knowledge of $D(T)/a^2$ for a sample, model ^{4}He profiles can be calculated according to radiogenic ingrowth, diffusion and α-ejection on specific t–T paths. A finite set of t–T paths will be consistent with the sample's ^{4}He distribution and He age. Running Monte Carlo simulations or using the constrained random search method [23] can identify a family of t–T solutions that are consistent with the ^{4}He profile. This approach is similar to that used with single-sample ^{40}Ar/^{39}Ar thermochronometry [24,25] and fission track length modeling [26].

3. Methods – simulations

To demonstrate the capabilities and limitations of this method, we simulated several step-heating experiments using Eq. 6. This complements a companion paper in which we apply the method to natural minerals [1]. For each step, we calculated remaining gas fractions f_i expected for various input concentration profiles $C_o(x)$ obtained from specified t–T paths. We explored the method's sensitivity both to the *shape* of an input concentration profile and also to the deficit gas fraction.

We used two approaches. The first was to input a known diffusivity function $D(T)/a^2$ and an arbitrary concentration profile $C_o(x)$, with which we calculated remaining fractions for each step of a simulated heating schedule. Using the set f_i, we simulated the fraction of gas released at each step:

$$F_i = f_{i-1} - f_i, \quad \text{where } f_o \equiv 1 \tag{13}$$

Using step release fractions, F_i, we calculated a set of $\ln(D/a^2)_{\text{calculated}}$ values using [12] by *inappropriately* assuming an initially uniform concentration profile. We plotted these values against

cumulative He release fraction (ΣF_i) to graphically represent characteristic $\ln(D/a^2)_{calculated}$ patterns.

The second approach was to simulate a ratio evolution experiment. We assumed a function $D(T)/a^2$ and two concentration profiles; one uniform (i.e., ^{3}He), the other arbitrarily round (i.e., ^{4}He). We calculated isotope ratios for each step from the release fractions (i.e., step $F_i^{4He}/F_i^{3He} = R_{step}$) and then normalized these ratios to the bulk ratio, R_{bulk}, calculated by integrating the initial profiles. The output is a plot of normalized ^{4}He/^{3}He vs. cumulative ^{3}He release fraction (ΣF^3He), or a *ratio evolution diagram*.

In both approaches, the release patterns ($\ln(D/a^2)_{calculated}$) vs. ΣF_i and R_{step}/R_{bulk} vs. ΣF^3He) reflect the input concentration profiles. The sensitivity that these output patterns have to the exact *shape* of the input profiles determines our ability to constrain actual concentration profiles by forward model matching.

In all calculations, we assumed ^{3}He and ^{4}He diffusivities to be identical. Some authors have suggested that the diffusion of a noble gas through a mineral may be governed by the kinetic theory of non-uniform gases resulting in mass-dependent diffusivities, (e.g., $D_4/D_3 = \sqrt{m_3/m_4} = 0.868$ [27,28]). While an effect of this magnitude has never been observed in minerals, other mass-dependent relationships may exist [29–31]. Because the thermally activated mobilization of a radiogenic noble gas through a solid is significantly different than most diffusive processes, it is not clear what mass dependence, if any, should relate diffusivities of the He isotopes. In a companion paper [1] we show that in apatite and titanite, diffusivities of spallation ^{3}He and radiogenic ^{4}He are equivalent within error, justifying our assumption. Nevertheless the above methods can easily be adjusted to accommodate a bias between ^{3}He and ^{4}He diffusivities if such is demonstrated for a given mineral.

Ejection of α-particles from the outer ~ 20 μm of a mineral causes a predictable shape to the radiogenic He profile independent of diffusion [32]. We initially ignored this effect, and then included it by assuming that the grain itself is the diffusion domain. Using a modified code of [33]

we calculated ^{4}He profiles by ingrowing radiogenic ^{4}He along a prescribed t–T path for a given diffusivity parameter set, with or without α-ejection. We simulated relatively simple but distinct t–T paths to assess how the resulting ^{4}He profiles and release patterns differ.

In the ingrowth calculations, we assumed a uniform parent distribution across the diffusion domain and a zero concentration boundary for all times t. For illustration, we used the best-fit diffusion parameters of Durango apatite for all simulations [13]. However, the ability to reconstruct concentration profiles is insensitive to the exact diffusion parameters used. For all calculations, we assumed spherical geometry and thermally activated volume diffusion from a single domain. Diffusion experiments have shown that individual grains of apatite, titanite and zircon can be well represented as single diffusion domains [13,14,34]. These simulations assume no measurement error.

While we have modeled He diffusion from minerals assuming spherical geometry, in reality the diffusion domain is unlikely to be a sphere. An important question is whether we can accurately capture diffusion behavior and resulting concentration profiles from a more realistic geometry (e.g., a cylinder [13,35]) using our model. In [1] we show that provided the diffusivities (from ^{3}He), the ^{4}He release fractions, and the thermal (t–T) modeling are determined on the same sample with the same geometric assumption, the problem can be accurately represented by the spherical model without knowledge of a. Using stepwise release data for a uniformly distributed gas (^{3}He), the formulation of [12] produces diffusivities corresponding to a model spherical domain (of radius a) with a surface area to volume ratio approximating that of the actual domain. Regardless of geometry we must also assume that diffusivity is crystallographically isotropic, which appears to be the case at least for apatite [13].

4. Results

4.1. Forward models
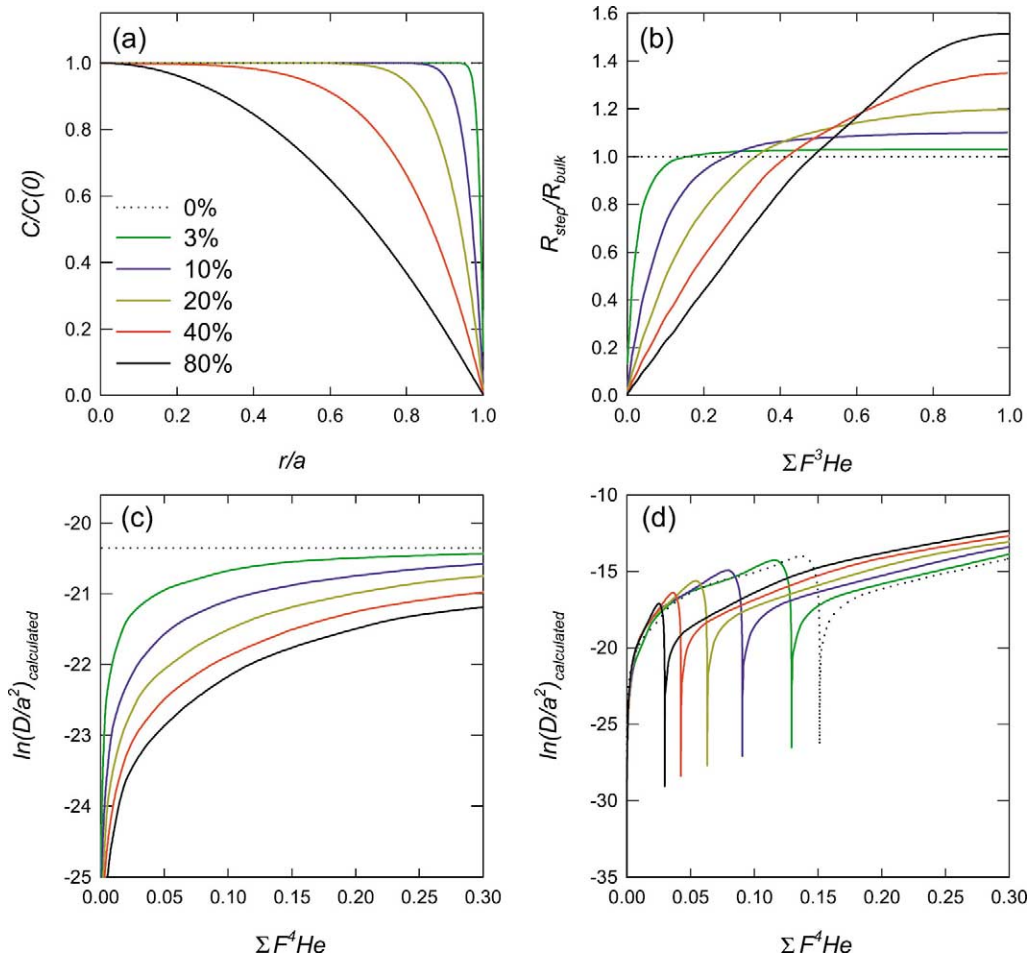
In this section, we show that specific t–T paths

Fig. 1. Stepwise outgassing simulation of isothermally evolved profiles. (a) Initial ^{4}He concentration, C (normalized to the concentration at the center of the domain, $C(0)$) at the radial position r (normalized to domain radius, a) within the spherical domain. The six concentration profiles shown were calculated according to isothermal accumulation and diffusion, excluding α-ejection. The color of each profile corresponds to a deficit gas fraction; labels in % indicate the deficit gas fraction of each curve. (b) Step-heating simulations plotted as a ratio evolution diagram. The simulations are shown as continuous functions, although calculated at discrete heating steps. (c,d) $\ln(D/a^2)_{calculated}$ values (according to Fechtig and Kalbitzer [12] assuming an initially uniform distribution) plotted vs. cumulative ^{4}He release fraction, ΣF^4He. Simulations in panel c were calculated using an isothermal heating schedule, those in panel d a heating schedule with a single thermal cycle (up-down-up).

result in specific ^{4}He concentration profiles. The absolute He concentration depends on the U and Th concentrations, but the *shape* of the ^{4}He profile depends only on thermal history and α-ejection. When run through simulated stepwise degassing experiments, the profiles yield distinct ^{4}He release patterns (Figs. 1–3). We present the results in order of increasing concentration profile complexity, i.e., in order of increasing radial structure.

4.1.1. Isothermal profiles

In Fig. 1, we present stepwise degassing simulations for six concentration profiles calculated according to ingrowth and diffusion under isothermal conditions, but excluding the effect of α-ejection. These represent relatively simple profiles expected in nature (e.g., for a surface-exposed sample, a low-temperature precipitate such as a weathering product [36] or biogenic fossil [37],
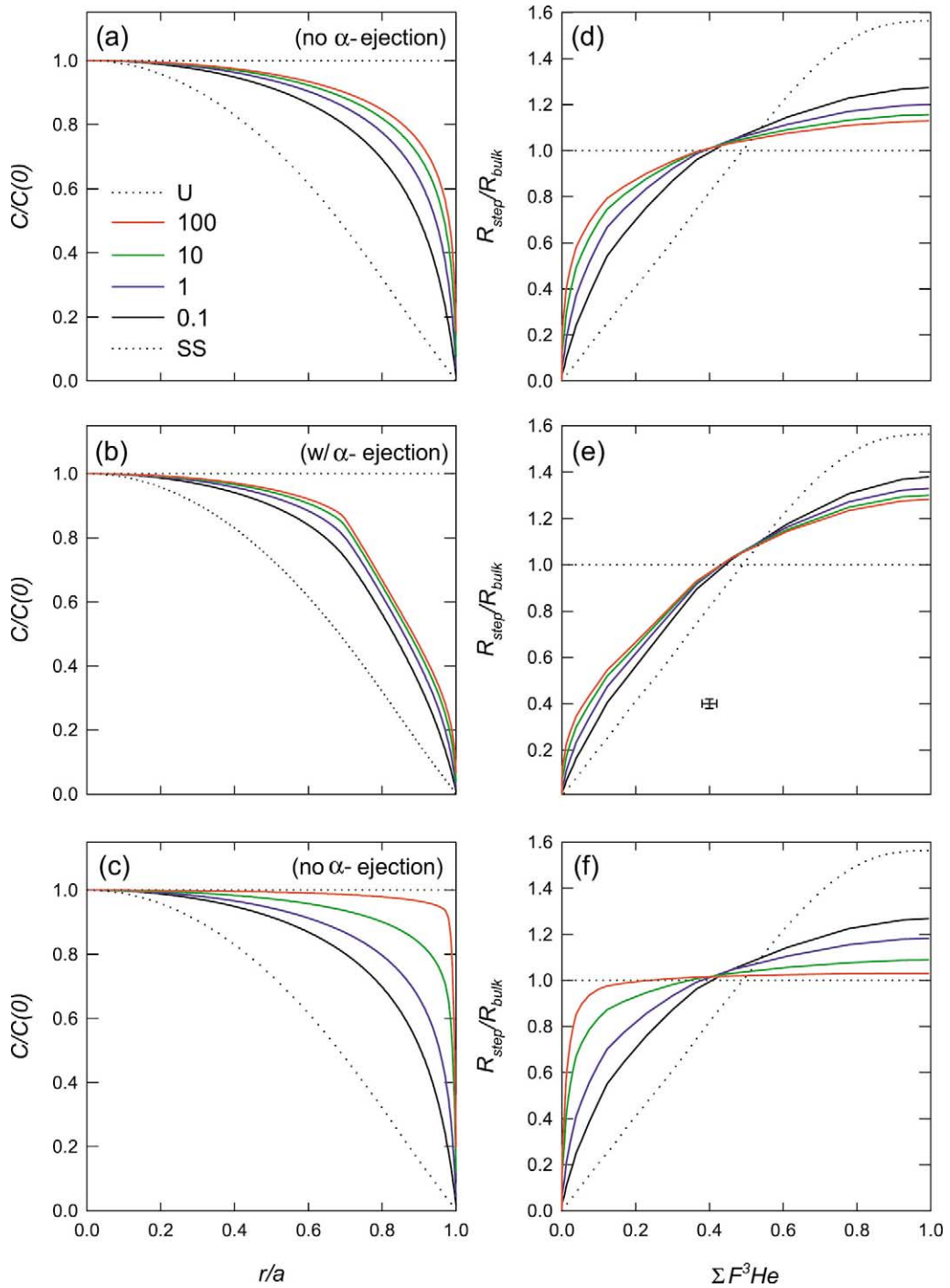
or certain meteoritic samples [38,39]). These profiles might represent ^{4}He distributions in six different minerals that are variably He-retentive or in one mineral calculated at six different constant temperatures; each curve reflects a unique $(D/a^2)t$ product. We simulated release patterns for each profile using an isothermal heating schedule (Fig. 1c) and a 'cycled' schedule (Fig. 1d) that includes steps of both increasing and decreasing (retrograde) temperature.

Each of these profiles produces a unique curve in the three output diagrams. Release fractions and isotope ratios for each step and for the bulk material are the observed quantities in the ratio evolution experiment and permit construction of the ratio evolution diagram (Fig. 1b). Although the values of discrete points along the curves in Fig. 1b depend on the function $D(T)/a^2$, the overall shape of a set of values reflects the concentration profile independent of diffusivity and heating schedule. Fig. 1c,d illustrates an alternative presentation of the same results. If a uniformly distributed isotope is not available, release fractions of only a diffusively rounded isotope distribution are measurable. If diffusion coefficients are calculated from a rounded profile (assuming an initially uniform profile), the calculated values, $\ln(D/a^2)_{\text{calculated}}$, will underestimate the true values according to the shape of the profile. This is an artifact of the invalidly assumed initial condition. If the actual $D(T)/a^2$ is known, this artifact can be used to constrain the shape of the profile by forward model matching in $\ln(D/a^2)_{\text{calculated}}$ vs. ΣF_i plotting space. Fig. 1c,d shows that the calculation is highly sensitive to the heating schedule. Retrograde temperature steps result in a particularly distinct pattern with which to match a model.

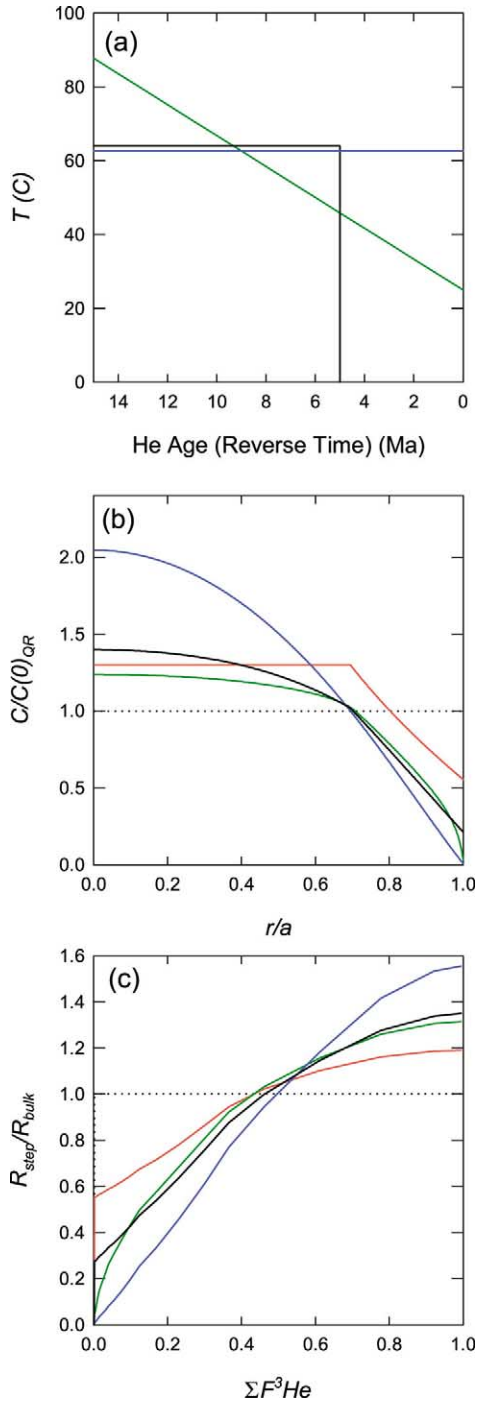### 4.1.2. Monotonic cooling

In Fig. 2d,e, we present step-heating simulations for a diffusion domain with $a = 65$ μm. Each simulation corresponds to a concentration profile calculated according to a constant cooling rate (0.1, 1, 10 and 100°C/Myr) from 125°C to 25°C. These represent concentration profiles that might be expected, e.g., in an exhuming mountain range. The profiles were calculated either excluding (Fig. 2a) or including (Fig. 2b) α-ejection. Each step-heating simulation used the isothermal heating schedule in Section 4.1.1.

In Fig. 2d, each of the profiles produces a distinct ratio evolution curve: faster cooling rates produce less rounded profiles (more He near the grain edge) and steeper trajectories on the ratio evolution diagram. The effects are most pronounced in the first ∼10–20% of gas released. Maximum differences between the curves occur at steps when $\Sigma F^3\text{He} \approx 10\%$.

In the absence of diffusion, α-ejection causes the He concentration profile to decline from unity to ∼0.4 (in $C/C(0)$ units) over the outermost ∼20 μm of the grain (e.g., see Fig. 3b). This pattern is distinct from all diffusive profiles in that it is non-zero at the grain edge. The ratio evolution for this profile (Fig. 3c) shows elevated ratios (compared to diffusion profiles) that increase nearly linearly up to $\Sigma F^3\text{He} \approx 30\%$. The effect of α-ejection combined with monotonic cooling is shown in Fig. 2b,e. The net effect of α-ejection is to induce a distinctive linearity to the first ∼30% of the ratio evolution plot. Although the profiles resulting from the different t–T paths are less distinct from each other, α-ejection does not eliminate the differences between them. As with the previous models, the maximum differences between the curves occurs when $\Sigma F^3\text{He} \approx 10\%$. Because α-ejection is temperature-independent, it can dominate the shape of a profile under fast cooling conditions (where diffusive rounding is small), but becomes less significant under slow cooling (where diffusive rounding is

---

←

Fig. 2. Step-heating simulations of profiles resulting from monotonic cooling. Concentration profiles are shown in panels a–c and the corresponding step-heating simulations shown as ratio evolution diagrams in panels d–f. The color of each curve corresponds to a particular cooling rate from 125°C to 25°C; labels are in units of °C/Myr. The t–T simulations used to calculate the profiles in panels a and b ended when the temperature reached 25°C and in panel c was followed by isothermal accumulation at 25°C for 5 Myr. Shown for reference are the quantitative retention uniform distribution (U) and steady state (SS) profile simulations (black dotted curves). The simulations presented in panels a and c were calculated excluding the effect of α-ejection.

high). The effect of α-ejection becomes increasingly large as domain size decreases toward the α-stopping range of ~ 20 μm. This implies that α-ejection may limit the recovery of t–T information from smaller grains.

4.1.3. Monotonic cooling followed by 5 Myr at 25°C

In many geologic situations, a sample will have experienced long-term cooling followed by a near-surface, quasi-isothermal period. One example is a rock exhumed on a normal fault that has become inactive. In Fig. 2c, concentration profiles were calculated according to a constant cooling rate (0.1, 1, 10 and 100°C/Myr) from 125°C to 25°C followed by 5 Myr of isothermal holding at 25°C.

The simulations in Fig. 2f are again distinct, with maximum differences at steps when $\Sigma F^3\text{He} \approx 10\%$. Comparing Fig. 2a and c illustrates that low-temperature isothermal holding causes a profile to become more 'square' and leads to greater retention of gas toward the domain edge. This is reflected in Fig. 2f as rapid ratio evolution in the initial steps of the ratio evolution diagram. The effect is greatest when a significant fraction of the gas is accumulated at temperatures where diffusion is negligible.

4.1.4. Distinct thermal histories for samples with a common He age

In Fig. 3, we present simulations of a diffusion

←

Fig. 3. Simulations of profiles obtained from distinct thermal histories yielding an apatite (U–Th)/He age of 10 Ma. The color of each curve corresponds to a specific accumulation model. The thermal histories are presented in panel a: instantaneous quenching at 10 Ma followed by quantitative retention at very low temperatures (< 20°C) for 10 Myr (with and without α-ejection; dotted black and red curve, respectively), isothermal holding at ~ 63°C for 100 Myr resulting in a steady-state ^{4}He distribution (blue curve), constant cooling from 88°C to 25°C over 15 Myr ($dC/dt = 4.2$°C/Myr; green curve), and isothermal holding at 64°C from 15 Ma to 5 Ma followed by instantaneous quenching to < 20°C at 5 Ma followed by quantitative retention for 5 Myr (solid black curve). The profiles, normalized as $C/C(0)_{QR}$ (where $C(0)_{QR}$ is the concentration at the center of the quantitative retention profile) are shown in panel b, and their corresponding ratio evolution diagrams are shown in panel c.
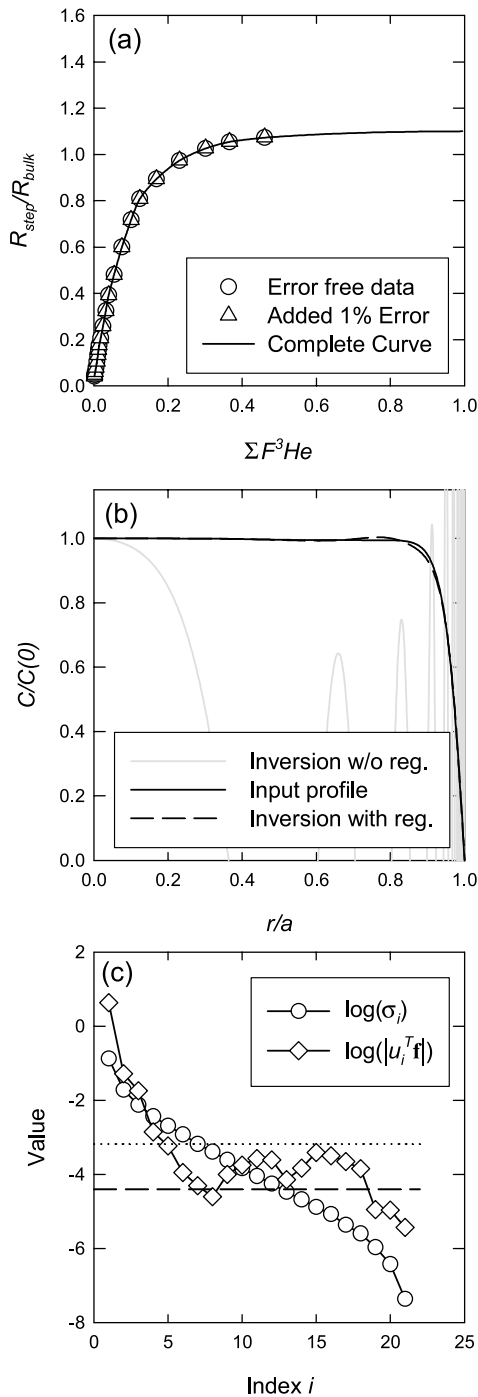
domain with $a = 65$ μm that experienced four very different thermal histories (Fig. 3a) that would each result in a 10 Ma He age. The resulting concentration profiles in Fig. 3b yield very distinct ratio evolution diagrams (Fig. 3c). For instance, although the profiles calculated according to linear cooling from 88°C to 25°C over 15 Myr (green curve) and isothermal holding at 64°C from 15 Ma to 5 Ma followed by instantaneous quenching to and quantitative retention at $< 20°C$ at 5 Ma (black curve) are similar, the ratios differ greatly when $\Sigma F^3He < 10\%$.

In an actual experiment, the bulk He age provides an important additional constraint on a sample's thermal history. In particular, when forward calculating model He profiles, the He age constrains the integrated ^4He abundance that is permitted within the domain for each potential geologic t–T path.

4.2. Inversions

In the absence of simulated analytical error, all of the ratio evolution diagrams in Section 4.1 could be inverted to recover the concentration profiles to within round-off error (not shown). However, once errors are included the inversion becomes unstable; the ridge regression is designed to filter the influence of these errors. The extent to which random errors affect the inversion depends on the complexity of the profile and the number and distribution (in ΣF^3He) of steps in the heating schedule. The inversion of more complicated re-

←

Fig. 4. Effects of a 1% error in measured He data on the profile obtained using the inversion method. (a) Ratio evolution plot of the simulated error free data (circles) and with added errors (triangles). (b) Input profile (solid black), the inverse solution of the error containing data calculated without regularization (solid gray) and the solution calculated with regularization (dashed black). (c) Singular-value spectrum for the error-containing dataset is shown. Shown are the logarithms of the singular values ($\log(\sigma_i)$; circles) and the absolute values of $|u_i^T\mathbf{f}|$ (see text; $\log(|u_i^T\mathbf{f}|)$; diamonds) each plotted vs. index number i. We minimized the influence of higher-order, error-dominated terms by using a threshold $i_h = 7$ which roughly corresponds to the regularization parameter $\log(h) = -3.18$ used in the inversion, shown as a dotted line.

lease patterns tolerates less error than simple profiles.

To illustrate the effect of error we added a normally distributed, random 1% error to 21 simulated ^{4}He and ^{3}He release fractions for the relatively simple 10% deficit profile calculated by isothermal ingrowth (Fig. 1a). We added errors to each release step, and then renormalized them according to their new sum. The results of this simulation and inversion are presented in Fig. 4. The solid gray curve in Fig. 4b was calculated with a regularization parameter $h = 0$, equivalent to inverting Eq. 9 *without* regularization (see [19]). The solution $\hat{\mathbf{b}}$ is clearly incorrect and illustrates that even a small amount of error can dramatically degrade the inverse solution.

The singular-value decomposition spectrum for this example is shown in Fig. 4c. For $i > 7$, the $\log(|u_i^T\mathbf{f}|)$ spectrum is approximately flat, indicating that these components and therefore the linear solution is dominated by high-frequency terms, which we assume are attributable to the added errors. By using a value $\log(h) = -3.18$ (corresponding to $i < 7$, dotted line in Fig. 4c) in Eq. 11, the error-dominated components are filtered from the linear combination according to Eq. 12. After regularization, the inverted profile is nearly equivalent to the input profile (Fig. 4b). The 1% errors used in this simulation are smaller than those anticipated in most stepwise experiments and hardly recognizable in the ratio evolution diagram (Fig. 4a). The difference between the solid gray and the dashed black curves clearly illustrates the importance of the ridge regression for inverting actual step release data. In our companion paper, we show that data containing more significant errors can also be successfully inverted [1].

5. Discussion

The modeling results shown above demonstrate that significant information can be obtained from step heating of a sample with a natural ^{4}He distribution and an artificial, homogeneous ^{3}He distribution. How well can the distribution be obtained, and how can we quantify the confidence of a constrained profile? Ultimately, the number of heating steps and their distribution (in ΣF^3He), and the precision and accuracy of the data determine what resolution a given experiment has for constraining a He distribution. This is easily recognized for forward model matching, although less obvious for the inversion technique. We discuss each separately below.

5.1. Forward model matching

The forward models presented in Section 4.1 most clearly illustrate the potential utility and limitations of using a ratio evolution experiment to constrain a natural ^{4}He distribution. The importance of measurement precision is clear in Figs. 1–3; e.g., typical differences are tens of percent in the ^{4}He/^{3}He ratio. Because the above calculations use release *fractions*, precision and response linearity are more important than the accuracy of a set of measurements.

Helium isotope ratios and ^{3}He relative abundances (i.e., ΣF^3He) can routinely be measured to better than 1% relative standard error on samples of interest for this work [1], so the curves in Figs. 1b, 2d,f and 3c should be easily resolvable from one another. A ratio evolution diagram provides a useful plotting space for forward model matching, and a set of measured values constrain a sample's unknown ^{4}He profile to within the analytical uncertainty of the set of measurements.

For increasingly large deficit gas fractions, the concentration profiles in Fig. 1 become less distinct. For instance, there is approximately equivalent difference in ^{4}He/^{3}He at a given ΣF^3He between the 10% and 20% deficit curves as there is between the 20% and 40% curves (Fig. 1b). The limiting case is the steady-state distribution in which radiogenic production and diffusive loss are balanced [33] shown in Fig. 5a. As this case is approached, differences become irresolvable, e.g., there is no obvious difference between 90% and 99% deficit curves. As a quantitative technique, stepwise degassing experiments have greatest sensitivity for constraining profiles with small deficit gas fractions ($< 40\%$). In all of the simulations, we find significant differences between val-
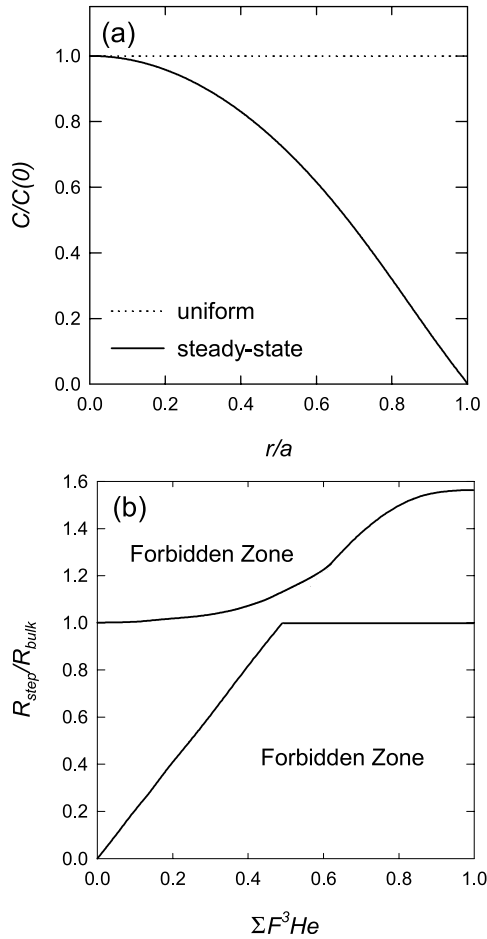
Fig. 5. Limits for the spatially uniform ^{4}He production–diffusion model. (a) The two limiting case concentration profiles: quantitative retention and steady state. (b) Ratio evolution diagram indicating allowed region for samples obeying uniform production–diffusion.

ues of R_{step}/R_{bulk} when $0\% < \Sigma F^3He < 20\%$. With knowledge of $D(T)a^2$, a heating schedule could be designed to maximize the number of steps in this range.

5.2. Inversion accuracy and resolution

The concentration profile obtained by inversion in Fig. 4b agrees well with the input profile, but not perfectly. Unfortunately, it is difficult to reliably estimate a confidence interval for the inverted profile due to the inability to accurately assign uncertainty to the regularization parame-

ter, h. High-frequency oscillation with respect to r, and zero crossings, would clearly indicate an unstable result. Given sufficient ^{3}He and ^{4}He abundances, the number of heating steps can be arbitrarily large, and the heating schedule could be designed for optimum inversion conditions. Therefore, measurement precision primarily limits the accuracy of an inverted concentration profile.

Because the confidence level of a He profile will ultimately determine the confidence in an inferred thermal history, it may be beneficial to consider both the shape of an inverted profile and the associated ratio evolution diagram (alternatively $\ln(D/a^2)_{calculated}$ vs. ΣF_i) to check for consistency. In some instances, it may be possible to better constrain a profile by comparing forward model calculations with the observed ratio evolution diagram without relying on the inversion.

The resolution kernels (rows of the resolution matrix; not shown) for the inverse calculation reveal important limitations to this approach [20]. As expected, the resolution kernels indicate maximum resolving power toward the outer edge of the diffusion domain. The inversion of stepwise outgassing data has greatest ability to 'observe' the concentration profile towards the edge of the diffusion domain, and least resolving power towards the domain's interior. Indeed, this is also found in our forward simulations.

The approximation used in the remaining gas fraction expression (Eq. 8) limits the maximum value of τ that can be inverted. This is problematic when inverting profiles with large deficit gas fractions because these more rounded profiles require larger values of τ at each step to evolve measurable quantities of ^{4}He. Because the approximation (Eq. 8) is only valid for $\tau_i < 0.05$, many data determined at the end of an experiment may not be usable in the inversion, although they would be observable in a ratio evolution diagram. To avoid this problem, an exact expression could be numerically integrated as an alternative to Eq. 8 (see [18,19]). Because the exact expression contains an infinite series, an acceptable numerical evaluation could require significantly more computation time.

Another interesting limitation to the inverse

calculation would result from a discontinuous concentration profile at the domain boundary. Inverting release fractions for a sample containing a discontinuity at $r/a = 1$, such as a uniform distribution, would result in a solution that contains high-frequency oscillations near $r/a = 1$ and an 'overshoot' analogous to the Gibbs phenomenon.

5.3. Plotting space

In Figs. 1 and 4b we show three ways to represent experimental results: (i) the ratio evolution diagram (R_{step}/R_{bulk} vs. ΣF^3He), (ii) a plot of $\ln(D/a^2)_{calculated}$ vs. ΣF_i, and (iii) the concentration profile obtained from inversion of the isotope data. There are advantages and disadvantages associated with each presentation.

The ratio evolution diagram most directly represents the measured quantities of an experiment. The diagram does not incorporate any artifacts associated with assumed initial conditions. The values are model-independent and the shape of a plot lacks D/a^2 dependence. For these reasons, the curves presented in Fig. 1b are independent of the heating schedule and are generally applicable for model matching. For instance, the ratio evolution diagram for a 10% deficit gas fraction profile calculated by isothermal accumulation will be the same for any mineral.

The ratio evolution diagram can also be used to test for validity of assumptions of the method. There are the two limiting case ^{4}He profiles for uniform production and diffusion: a uniform profile (quantitative retention) and a steady-state distribution (Fig. 5a). Every other profile must plot between these two limits (Fig. 5b) and not in the 'forbidden zones'. This is also true if α-particles have been ejected from the domain. The ratio evolution diagram can thus be used to test for spatial heterogeneity of He production. If values plot within either of the 'forbidden zones', the ^{4}He distribution does not smoothly decrease outward toward the domain's edge as is required by diffusion and α-ejection alone. For values $\Sigma F^3He < 0.5$, points plotting in the upper forbidden zone indicate ^{4}He excess toward the domain's edge, while those in the lower forbidden zone in-

dicate ^{4}He excess toward the domain's interior. The converse statements are generally true for $\Sigma F^3He > 0.5$. Since a strongly heterogeneous ^{4}He distribution likely reflects the parent nuclide distribution, the plot may identify non-uniform U and/or Th distributions, mineral inclusions or α-implantation at the edge of the domain. Values plotting in a forbidden zone are a sufficient but not necessary condition for identification of these effects.

A plot of $\ln(D/a^2)_{calculated}$ vs. ΣF_i can alternatively be used if a uniformly distributed isotope is not available. The values in this plot are model-dependent and the shape depends strongly on the function $D(T)/a^2$ and the heating schedule. If calculated for a non-uniform initial profile, the diffusion coefficients will be incorrect. However, the plot provides a high-resolution plotting space for forward model matching. In some cases, it may be possible to constrain the function $D(T)/a^2$ and the shape of a profile from a single analysis. For instance, as a rounded profile evolves throughout an experiment, the $\ln(D/a^2)_{calculated}$ values approach the true values at a given temperature (Fig. 1c). For samples with relatively small deficit gas fractions ($< 20\%$), the true $\ln(D/a^2)$ values are reasonably approximated when $\Sigma F \approx 0.75$. For the 3%, 10% and 20% deficit curves in Fig. 1c the ratio of $(D/a^2)_{calculated}$ to $(D/a^2)_{true}$ is 0.99, 0.97, and 0.95, respectively when $\Sigma F = 0.75$.

The inverted spherical profile plot (i.e., Fig. 4b) is the most readily interpretable presentation for describing a He distribution. However, as discussed above, it is susceptible to slight measurement inaccuracies and filtering bias.

Throughout this paper, we have focused on constraining the shape of a ^{4}He profile. With the exception of the ratio evolution experiment, the methods above are also suitable for determining the shape of a natural ^{3}He profile. A two-aliquot experiment could potentially constrain a rounded cosmogenic ^{3}He profile: one irradiated aliquot for determining $D(T)/a^2$, the other for the profile. The irradiated aliquot would have to have sufficient ^{3}He added to make the initial abundance negligibly small. Forward production–diffusion calculations assuming a uniform cosmogenic ^{3}He production rate could

be used to generate model ^{3}He profiles for comparison.

5.4. Correcting (U–Th)/He ages

Samples that have experienced only modest diffusive loss since He retention began have concentration profiles that include a nearly invariant segment in the core of the domain. This is revealed on the ratio evolution diagram by invariance in the ^{4}He/^{3}He ratio at high cumulative ^{3}He yields (e.g., the 3% and 10% deficit fraction curves in Fig. 1b), much like the plateau in a ^{40}Ar/^{39}Ar analysis. Under these conditions the deficit gas fraction can be used to correct the (U–Th)/He age for diffusive loss: corrected He content = measured content ÷ (1−deficit gas fraction). This procedure inherently includes α-ejection losses, so eliminates the need to make a geometry-based ejection correction. The plateau approach makes most sense for partially retentive samples that have experienced isothermal conditions since formation, e.g., volcanic phenocrysts and chemical precipitates, and for those samples with ambiguous α-ejection correction (see [8] for an example of ambiguity).

5.5. Constraining thermal histories

The simulations shown in Figs. 2 and 3 indicate that ratio evolution experiments could constrain thermal histories from the analysis of just one crystal or a population of size-sorted crystals. This capability holds great potential for thermochronometry, where constraining cooling rates currently requires model-dependent interpretation of a number of He ages from a given area, e.g., in a vertical sampling traverse. With the profiling method it would be possible to ascertain the same information from just one sample, and by analyzing several samples of different He age, it would be possible to obtain greater temporal resolution on the cooling rate. With additional chronological or geologic evidence, a ^{4}He concentration profile could be used to more narrowly constrain a sample's thermal history. The most basic additional constraint is the (U–Th)/He age.

It is critically important that the forward thermal models use the function $D(T)/a^2$ that is specific to the sample. The experimentally determined diffusivity, D, and the characteristic length scale, a, specify the sample. By transforming a problem of profile model matching to the spherical domain, the two parameters are inextricably linked. Modeled profiles, determined through forward calculation, must contain each. Application of a specific experimentally determined function $D(T)/a^2$ (e.g., for Durango apatite) to an unstudied specimen possibly of a different grain size must be done with caution.

It is also important to recognize that the technique we describe in this paper constrains the shape of a He profile, and not a thermal history. Once a profile is determined it can then be used to constrain the possible t–T paths that are consistent with its shape. Although the simulations presented in Section 4.1 uniquely resolved the concentration profiles corresponding to each t–T path, they did not *uniquely* constrain the cooling rates and thermal histories. For instance, the profiles and release patterns in Fig. 2c,f have similar shapes as those in Fig. 1a,b, despite having different t–T paths. As thermal histories become increasingly complex, their resulting concentration profiles less uniquely reflect the corresponding t–T path. There will always be multiple thermal histories consistent with a given profile.

6. Conclusion

The ability to generate a uniform ^{3}He distribution within minerals [1] permits a variety of new applications for He isotope geochemistry. Most simply, it permits He diffusivity measurements of samples which have insufficient natural He for such measurement, or in samples in which the natural concentration distribution is non-uniform. For samples with a measurable amount of natural ^{4}He, variations in the ^{4}He/^{3}He ratio over the course of a stepwise heating experiment reflect the initial ^{4}He distribution within the sample. Both forward and inverse modeling can be used to constrain these profiles, which can in turn be used to: (i) correct He ages for diffusion and

α-ejection losses in some circumstances, and (ii) constrain the *t–T* path of the sample.

Acknowledgements

References

[1] D.L. Shuster, K.A. Farley, J.M. Sisterson, D.S. Burnett Quantifying the diffusion kinetics and spatial distributions of radiogenic ^{4}He in minerals containing proton-induced ^{3}He, Earth Planet. Sci. Lett. 217 (2004) 19–32, this issue.

[2] P.M. Hurley, The helium age method and the distribution and migration of helium in rocks, in: P.M. Hurley (Ed.), The Helium Age Method and the Distribution and Migration of Helium in Rocks, Nuclear Geology, Wiley, New York, 1954, pp. 301–329.

[3] P.K. Zeitler et al., U–Th–He dating of apatite: a potential thermochronometer, Geochim. Cosmochim. Acta 51 (1987) 2865–2868.

[4] J.T. Wasson, S. Wang, The histories of ordinary chondrite parent bodies – U, Th–He age distributions, Meteoritics 26 (1991) 161–167.

[5] K.A. Farley, (U–Th)/He dating: Techniques, calibrations, and applications, in: D. Porcelli, C.J. Ballentine, R. Wieler (Eds.), Reviews in Mineralogy and Geochemistry: Noble Gases in Geochemistry and Cosmochemistry, 2002, pp. 819–844.

[6] S. Niedermann, Cosmic-ray-produced noble gases in terrestrial rocks: Dating tools for surface processes, in: D. Porcelli, C.J. Ballentine, R. Wieler (Eds.), Reviews in Mineralogy and Geochemistry: Noble Gases in Geochemistry and Cosmochemistry, 2002, pp. 731–777.

[7] R. Wieler, Cosmic-ray-produced noble gases in meteorites, in: D. Porcelli, C.J. Ballentine, R. Wieler (Eds.), Reviews in Mineralogy and Geochemistry: Noble Gases in Geochemistry and Cosmochemistry, 2002, pp. 125–163.

[8] K.A. Farley, B.P. Kohn, B. Pillans, (U–Th)/He dating of Pleistocene zircon and apatite: A test case from the Rangitawa tephra, North Island, New Zealand, Earth Planet. Sci. Lett. (2002) (in press).

[9] D. Gosset, P. Trocellier, Y. Serruys, Determination of the helium diffusion coefficient in nuclear waste storage ceramics by a nuclear reaction analysis method, J. Nucl. Mater. 303 (2002) 115–124.

[10] T. Dunai, K. Roseleib, Sorption and diffusion of helium in garnet; implications for volatile tracing and dating, Earth Planet. Sci. Lett. 139 (1996) 411–421.

[11] T.W. Trull, M.D. Kurz, W.J. Jenkins, Diffusion of cosmogenic ^{3}He in olivine and quartz: implications for surface exposure dating, Earth Planet. Sci. Lett. 103 (1991) 241–256.

[12] H. Fechtig, S. Kalbitzer, The diffusion of argon in potassium bearing solids, in: O.A. Schaeffer, J. Zähringer (Eds.), Potassium-Argon Dating, Springer, Heidelberg, 1966, pp. 68–106.

[13] K.A. Farley, Helium diffusion from apatite: general behavior as illustrated by Durango fluorapatite, J. Geophys. Res. 105 (2000) 2903–2914.

[14] P.W. Reiners, K.A. Farley, Helium diffusion and (U–Th)/He thermochronometry of titanite, Geochim. Cosmochim. Acta 63 (1999) 3845–3859.

[15] I. McDougall, T.M. Harrison, Geochronology and Thermochronology by the ^{40}Ar/^{39}Ar Method, 2nd edn., Oxford Monographs on Geology and Geophysics, 1999, 269 pp.

[16] S.P. Kelley, J.-A. Wartho, Rapid kimberlite ascent and the significance of Ar–Ar ages in xenolith phlogopites, Science 289 (2000) 609–611.

[17] F. Albarède, The recovery of spatial isotope distributions from stepwise degassing data, Earth Planet. Sci. Lett. 39 (1978) 387–397.

[18] H.S. Carslaw, J.C. Jaeger, Conduction of Heat in Solids, 2nd edn., Oxford University Press, New York, 1959, 510 pp.

[19] F. Albarède, Introduction to Geochemical Modeling, Cambridge University Press, Cambridge, 1996, 543 pp.

[20] P.C. Hansen, Rank-deficient and discrete ill-posed problems: numerical aspects of linear inversion. SIAM Monographs on Mathematical Modeling and Computation, 1998, Philadelphia, PA, 247 pp.

[21] A.E. Hoerl, R.W. Kennard, Ridge regression – biased estimation for nonorthogonal problems, Technometrics 12 (1970) 55.

[22] A.E. Hoerl, R.W. Kennard, Ridge regression – applications to nonorthogonal problems, Technometrics 12 (1970) 69.

[23] S.D. Willett, Inverse modeling of annealing of fission tracks in apatite 1: A Controlled Random Search method, Am. J. Sci. 297 (1997) 939–969.

[24] F.M. Richter et al., Tibetan tectonics from ^{40}Ar/^{39}Ar analysis of a single K-feldspar sample, Earth Planet. Sci. Lett. 105 (1991) 266–278.

[25] X. Quidelleur et al., Thermal evolution and slip history of the Renbu Zedong Thrust, southeastern Tibet, J. Geophys. Res. Solid Earth 102 (1997) 2659–2679.

[26] K. Gallagher, Evolving temperature histories from apatite fission-track data, Earth Planet. Sci. Lett. 136 (1995) 421–435.

[27] I. Kaneoka, Rare gas isotopes and mass fractionation: an

indicator of gas transport into or from a magma, Earth Planet. Sci. Lett. 48 (1980) 284–292.

[28] S.R. Hart, Helium diffusion in olivine, Earth Planet. Sci. Lett. 70 (1984) 297–302.

[29] M.J. Murphy, G.A. Voth, A.L.R. Bug, Classical and quantum transition state theory for the diffusion of helium in silica sodalite, J. Phys. Chem. B 101 (1997) 491–503.

[30] T.W. Trull, M.D. Kurz, Experimental measurements of ^{3}He and ^{4}He mobility in olivine and clinopyroxene at magmatic temperatures, Geochim. Cosmochim. Acta 57 (1993) 1313–1324.

[31] T.W. Trull, M.D. Kurz, Isotopic fractionation accompanying helium diffusion in basaltic glass, J. Mol. Struct. 485 (1999) 555–567.

[32] K.A. Farley, R.A. Wolf, L.T. Silver, The effects of long alpha-stopping distances on (U–Th)/He ages, Geochim. Cosmochim. Acta 60 (1996) 4223–4229.

[33] R.A. Wolf, K.A. Farley, D.M. Kass, Modeling of the temperature sensitivity of the apatite (U–Th)/He thermochronometer, Chem. Geol. 148 (1998) 105–114.

[34] T. Tagami, K.A. Farley, D.F. Stockli, Thermal sensitivities of zircon (U–Th)/He and fission-track systems, Geochim. Cosmochim. Acta 67 (Suppl. 1) (2003) A466.

[35] A.G.C.A. Meesters, T.J. Dunai, Solving the production-diffusion equation for finite diffusion domains of various shapes: Part I. Implications for low-temperature (U–Th)/He thermochronology, Chem. Geol. 186 (2002) 333–344.

[36] D. Shuster, K.A. Farley, P. Vasconcelos, Geochronology of weathering processes by (U–Th)/He analysis of supergene goethite and cryptomelane, EOS Abstr. 81 (2000) 1263.

[37] K.A. Farley, T.E. Cerling, P.G. Fitzgerald, Cosmogenic He-3 in igneous and fossil tooth enamel fluorapatite, Earth Planet. Sci. Lett. 185 (2001) 7–14.

[38] B.P. Weiss, D.L. Shuster, S.T. Stewart, Temperatures on Mars from Ar-40/Ar-39 thermochronology of ALH84001, Earth Planet. Sci. Lett. 201 (2002) 465–472.

[39] K. Min et al., Single grain (U–Th)/He ages from phosphates in Acapulco meteorite and implications for thermal history, Earth Planet. Sci. Lett. 209 (2003) (in press).